Available online at www.sciencedirect.com
ScienceDirect
Trans. Nonferrous Met. Soc. China 33(2023) 95−106
Transactions of Nonferrous Metals Society of China
www.tnmsc.cn

Ductile fracture prediction of ZK61M high-strength magnesium alloy sheet during hot deformation process

Liu YANG[1,2], Yong-chuan DUAN[1,2], Ying-ping GUAN[1,2]

1. Key Laboratory of Advanced Forging & Stamping Technology and Science of Ministry of Education, Yanshan University, Qinhuangdao 066004, China;
2. School of Mechanical Engineering, Yanshan University, Qinhuangdao 066004, China

Received 29 October 2021; accepted 2 March 2022

Abstract: To predict the ductile fracture behavior of a ZK61M high-strength magnesium alloy sheet during hot deformation, experiments and numerical simulations were performed under specific conditions. According to the stress state parameters and fracture strain data obtained for different specimens, the undetermined coefficients of four fracture models were solved using the particle swarm optimization algorithm. According to the error evaluation results, the modified Wilkins model was the most accurate. This model was introduced into a finite element, and the results were compared with experimental results. The results indicated that the mean relative errors of the fracture displacement and fracture load of the tensile parts were <15%, and the mean relative error of the forming depth of the cylindrical parts was 13.88%. The established finite element model can accurately simulate the experimental process and predict the fracture position.

Key words: ZK61M sheet; ductile fracture model; parameter optimization; hot deformation; cylindrical part

1 Introduction

High-strength magnesium alloys have broad application prospects in the aerospace field due to their high specific strength and low density [1,2]. However, the plastic behavior of high-strength magnesium alloys is not exactly the same as that of traditional metals (steel, aluminum, etc) [3−5]. It is difficult to predict the fracture of high-strength magnesium alloys during hot deformation. Therefore, it is important to study the fracture behavior of high-strength magnesium alloys.

Ductile fracture models can be used to predict the failure behavior of metal during deformation. With the improvement of finite element numerical simulation technology and experimental conditions, ductile fracture models have been developed rapidly [6−8]. In recent years, there have been abundant research results on the fracture prediction of medium- and low-strength magnesium alloys. Scholars [9−11] have predicted the damage evolution laws of the AZ31 magnesium alloy during hot forming using coupled fracture models. Compared with coupled fracture models, uncoupled fracture models are easier to solve and integrate with finite element software and are more efficient for predicting fractures. For instance, the Freudenthal model was used to predict crack initiation and processing limits in the rolling and extrusion processes for the AZ31 magnesium alloy [12,13]. The Cockcroft–Latham, Brozzo, Ayada, and Clift models are also widely used in stamping and performance prediction [14−16]. The researches [17,18] have indicated that the stress state significantly affects the fracture of materials. XIAO et al [19] and HABIB et al [20] investigated magnesium alloy sheets at room temperature and

Corresponding author: Yong-chuan DUAN, Tel: +86-13230309697, E-mail: yongchuan.duan@ysu.edu.cn
DOI: 10.1016/S1003-6326(22)66093-X

accurately predicted the fracture behavior under different stress states. However, magnesium alloys are still mainly formed by hot working; thus, they have high temperature sensitivity and strain rate sensitivity. Hence, the hot deformation fracture model under different stress states has numerous parameters, which increases the difficulty of fracture prediction. At present, researchers still focuse on the fracture behavior analysis of medium- and low-strength magnesium alloys [21−24]. The research on hot ductile fracture of high-strength magnesium alloy sheets is insufficient.

In this study, a ZK61M sheet was used as the research material to predict fracture during hot deformation. First, the stress state parameters and fracture strain data under different deformation conditions were obtained. Then, the undetermined parameters of each fracture model were obtained using an optimization algorithm. According to the error evaluation method, a fracture model with a high prediction accuracy was determined. Finally, the fracture model was introduced into the finite element simulation to predict and analyze the fracture behavior in the process of hot deformation. The results can be used as a reference for the hot forming simulation of high-strength magnesium alloy sheets.

2 Fracture models

The stress state of a point can be determined by $(\bar{\sigma},\ \eta,\ \bar{\theta})$, and the fracture behavior of the material can be expressed using a three-dimensional space composed of the fracture strain, stress triaxiality, and Lode angle parameter, i.e., $(\bar{\varepsilon}_{\mathrm{f}},\ \eta,\ \bar{\theta})$. The fracture strain can be measured as the equivalent plastic strain before fracture, that is, $\bar{\varepsilon}_{\mathrm{f}}=\bar{\varepsilon}_{\mathrm{p}}$. The relationships among the principal stress (σ_1, σ_2, σ_3) and stress invariants (σ_{m}, η, θ) [25,26] are shown in Eqs. (1)−(3):

$$\eta=\frac{\sigma_{\mathrm{m}}}{\bar{\sigma}} \tag{1}$$

$$\bar{\theta}=1-\frac{6\theta}{\pi}=1-\frac{2}{\pi}\arccos\xi \tag{2}$$

$$\xi=\frac{27}{2}\frac{(\sigma_1-\sigma_{\mathrm{m}})(\sigma_2-\sigma_{\mathrm{m}})(\sigma_3-\sigma_{\mathrm{m}})}{\bar{\sigma}^3} \tag{3}$$

where σ_{m} represents the average stress, $\bar{\sigma}$ represents the equivalent stress, θ represents the Lode angle, and ξ represents the normalized third deviatoric stress.

To obtain a ductile fracture model that can describe the hot deformation characteristics of the ZK61M high-strength magnesium alloy, four uncoupled fracture models considering the stress triaxiality η and Lode angle parameter $\bar{\theta}$ are selected for analysis. The models are given by Eqs. (4)−(7).

Modified McClintock model: BAI and WIERZBICK [27] modified McClintock model [28] and obtained the following fracture model:

$$\bar{\varepsilon}_{\mathrm{f}}=\left[2/\sqrt{3}(1-n)D_{\mathrm{c}}\right]/\left\{\sinh\left\{\sqrt{3}(1-n)[\eta-1/3\cos(\pi/6(\bar{\theta}+7))]\right\}+(1-n)\sin(\pi/6(\bar{\theta}+1))\right\} \tag{4}$$

where D_{c} is an undetermined parameter and n is the hardening exponent.

Modified Cockcroft–Latham model: Under the assumption of material proportional loading, OH et al [29] modified Cockcroft–Latham model [30] and obtained the following fracture model:

$$\bar{\varepsilon}_{\mathrm{f}}=\frac{D_{\mathrm{c}}\bar{\sigma}}{\sigma_1}=\frac{3D_{\mathrm{c}}}{3\eta+2\cos\left(\pi/6\left(1-\bar{\theta}\right)\right)} \tag{5}$$

Bai–Wierzbicki model: Assuming that the ductility of materials is identical under the axisymmetric tensile and compressive stress, the Bai–Wierzbicki model [31] is obtained as follows:

$$\bar{\varepsilon}_{\mathrm{f}}=\left(D_1\mathrm{e}^{(-D_2\eta)}-D_3\mathrm{e}^{(-D_4\eta)}\right)\bar{\theta}^2+D_3\mathrm{e}^{(-D_4\eta)} \tag{6}$$

where D_1, D_2, D_3, and D_4 are the parameters to be determined.

Modified Wilkins model: Considering the influence of the hydrostatic pressure on the fracture performance of materials, the approximate Wilkins model [32] is

$$\bar{\varepsilon}_{\mathrm{f}}\approx D_{\mathrm{c}}\left(1-c_1\eta\right)^{\lambda}\left[2-\frac{\sin(|\bar{\theta}|\pi/6)}{\cos((1+|\bar{\theta}|)\pi/6)}\right]^{-\mu} \tag{7}$$

where c_1, λ, and μ are the parameters to be determined.

3 Calculation of fracture parameters

3.1 Tensile tests

The material used for testing was a ZK61M sheet with a thickness of 1.4 mm after extrusion and rolling. The chemical composition of this material

is presented in Table 1. Four types of tensile specimens were designed, as shown in Fig. 1. The specimens were cut along the rolling direction via wire cutting. Tensile tests were performed at deformation temperatures of 393, 423, 453, and 483 K and strain rates of 0.003, 0.01, 0.03 and 0.1 s^{-1}. The time when the first macrocrack appeared was defined as the fracture initiation time.

Table 1 Chemical composition of ZK61M magnesium alloy sheet (wt.%)

Mg	Zn	Zr	Al	Mn
Bal.	5.60	0.52	0.0012	0.011
Fe	Si	Cu	Ni	
0.0027	0.0036	0.0011	0.0016	

3.2 Constitutive model fitting

True stress–strain data calculated using the traditional formula are not suitable for describing the necked curve. The true stress–strain data in the instability section of hot tensile deformation are described by the Swift hardening function [33], as follows:

$$\bar{\sigma} = K(\varepsilon_y + \bar{\varepsilon}_p)^n \quad (8)$$

where K is the strength coefficient, ε_y represents the yield point strain, and $\bar{\varepsilon}_p$ represents the equivalent plastic strain.

According to the Swift hardening function, the true stress–strain data of flat smooth specimens under different deformation conditions were nonlinearly fitted. The fitted curves are shown in Fig. 2, and the parameter values of the fitted model are presented in Table 2.

To validate the fitting curve of the Swift hardening function, ABAQUS/Explicit software was used for finite element modeling and analysis. The boundary conditions were identical to those used in the tensile tests. One end was fixed, and the other end was subject to displacement constraints. An 8-node hexahedral linear reduced integral element (C3D8R) was selected for meshing. A comparison between the load–displacement curves of the simulation and the experiment for the flat smooth specimen is presented in Fig. 3(a). As shown, the curve based on the Swift hardening function agreed with the experimental curve, indicating that the function can be used to predict the plastic mechanical behavior of flat smooth specimens under axisymmetric tensile stress.

However, when the other three types of specimens (arc notch, shear notch, and tension−shear notch) were simulated, the obtained curves differed significantly from the experimental curves. The Swift hardening function cannot accurately simulate notch specimens. After repeated trial calculations, it was discovered that a curve consistent with the experiment could be obtained after adjusting the strength coefficient K and hardening index n in the Swift hardening function, as follows:

$$\bar{\sigma} = f_1 K(\varepsilon_y + \bar{\varepsilon}_p)^{f_2 n} \quad (9)$$

where f_1 and f_2 are adjustment coefficients.

Table 3 presents the values of the adjustment coefficients f_1 and f_2 at a strain rate of 0.03 s^{-1}. Figures 3(b−d) present load–displacement curves

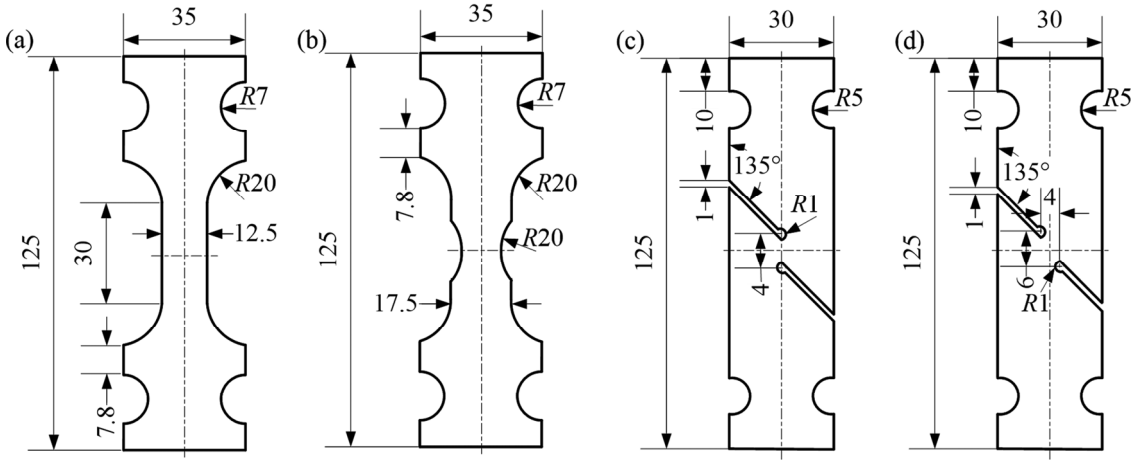

Fig. 1 Dimensions of different types of tensile specimens: (a) Flat smooth; (b) Arc notch; (c) Shear notch; (d) Tension−shear notch (Unit: mm)

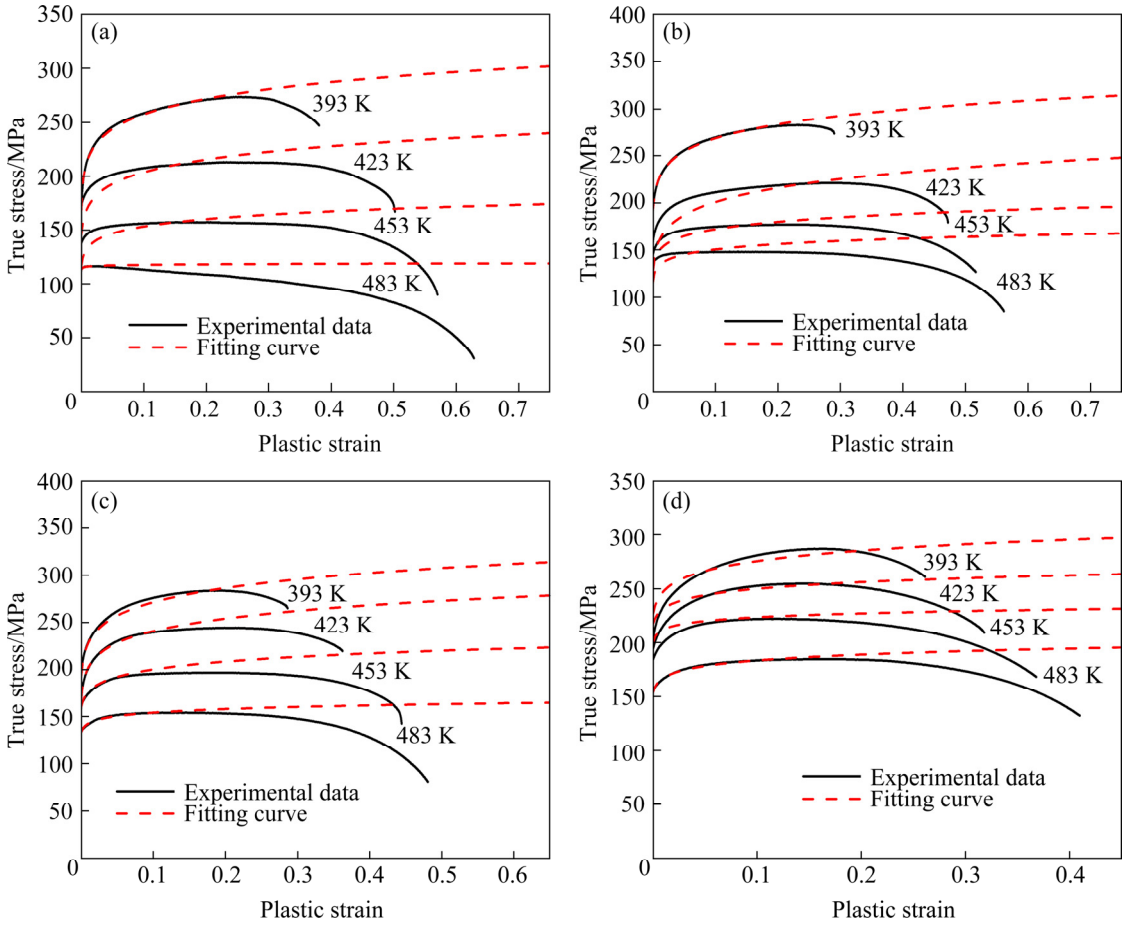

Fig. 2 True stress–strain curves of flat smooth specimens fitted under different conditions: (a) 0.003 s^{-1}; (b) 0.01 s^{-1}; (c) 0.03 s^{-1}; (d) 0.1 s^{-1}

Table 2 Parameter values of Swift hardening function after fitting

Temperature/K	Strain rate/s^{-1}	K/MPa	ε_y	n
393	0.003	308.94	0.00047	0.07921
	0.01	321.17	0.00133	0.07818
	0.03	324.75	0.00140	0.07845
	0.1	309.55	0.00210	0.05045
423	0.003	245.49	0.00160	0.09342
	0.01	255.67	0.00155	0.10511
	0.03	287.96	0.00109	0.07799
	0.1	271.13	0.00206	0.03547
453	0.003	177.46	0.00131	0.06340
	0.01	199.79	0.00085	0.06447
	0.03	229.13	0.00244	0.05924
	0.1	235.83	0.00069	0.02296
483	0.003	119.38	0.00028	0.00592
	0.01	170.28	0.00066	0.05316
	0.03	167.40	0.00187	0.03544
	0.1	202.23	0.00156	0.04219

of the simulation and experiment for the arc notch, shear notch, and tension-shear notch, respectively. As shown, the simulation and experimental curves agreed for the different types of notch specimens under various deformation conditions.

3.3 Stress state parameters

The maximum equivalent plastic strain at fracture was taken as the critical element, and the stress state parameters (stress triaxiality η and Lode angle parameter $\bar{\theta}$) of the critical element were extracted. Figure 4 presents the variation history curves of the stress triaxiality and Lode angle parameter for specimens with different shapes at 0.03 s^{-1} and 453 K. As shown, the stress triaxiality and Lode angle parameter constantly changed throughout the entire process from loading to fracture. Therefore, the average stress triaxiality η_{avg} and average Lode angle parameter $\bar{\theta}_{avg}$ were used to describe the stress state of the material, as follows [34]:

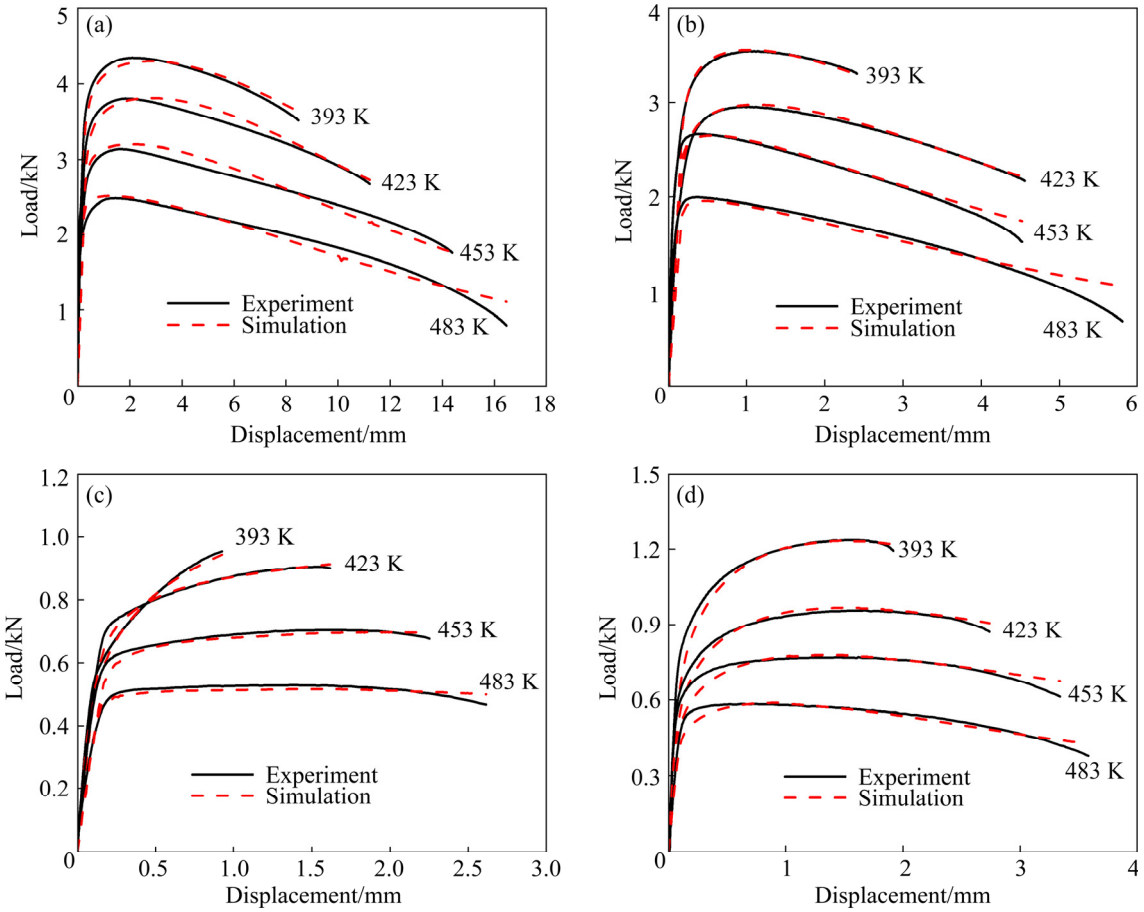

Fig. 3 Simulation and experimental load–displacement curves of specimens at 0.03 s^{-1}: (a) Flat smooth; (b) Arc notch; (c) Shear notch; (d) Tension−shear notch

Table 3 Values of adjustment coefficient at 0.03 s^{-1}

Adjustment coefficient	Arc notch				Shear notch				Tension−shear notch			
	393 K	423 K	453 K	483 K	393 K	423 K	453 K	483 K	393 K	423 K	453 K	483 K
f_1	0.99	0.95	0.92	0.90	1.16	1.00	0.93	0.93	0.86	0.75	0.73	0.59
f_2	1.10	1.20	0.73	0.90	2.50	1.20	0.91	0.60	2.00	2.00	2.27	1.00

$$\eta_{\text{avg}}=\frac{1}{\bar{\varepsilon}_{\text{f}}}\int_0^{\bar{\varepsilon}_{\text{f}}}\eta(\bar{\varepsilon}_{\text{p}})\text{d}\bar{\varepsilon}_{\text{p}} \tag{10}$$

$$\bar{\theta}_{\text{avg}}=\frac{1}{\bar{\varepsilon}_{\text{f}}}\int_0^{\bar{\varepsilon}_{\text{f}}}\bar{\theta}(\bar{\varepsilon}_{\text{p}})\text{d}\bar{\varepsilon}_{\text{p}} \tag{11}$$

where $\eta(\bar{\varepsilon}_{\text{p}})$ represents the variation history of the stress triaxiality η with respect to the equivalent plastic strain $\bar{\varepsilon}_{\text{p}}$, and $\bar{\theta}(\bar{\varepsilon}_{\text{p}})$ represents the variation history of the Lode angle parameter $\bar{\theta}$ with respect to the equivalent plastic strain $\bar{\varepsilon}_{\text{p}}$.

4 Optimization and validation

4.1 Optimization of undetermined parameters

Owing to the large number of experimental groups under different deformation conditions and different stress state combinations, the dispersion degree of the fracture data is significant. To select a more suitable fracture model, the particle swarm optimization algorithm was used to obtain the undetermined parameters [35,36]. The toolbox in MATLAB was used for optimization, and the optimal parameters were obtained using the minimum mean absolute error as the optimization objective. The surface fitting accuracy and model prediction accuracy were evaluated via a Chi-square test and the mean relative error:

$$\delta_{\text{mina}}=\min\left[\frac{1}{N}\sum_{i=1}^{N}\left|\bar{\varepsilon}_{\text{f},i}^{\text{fit}}-\bar{\varepsilon}_{\text{f},i}^{\text{exp}}\right|\right] \tag{12}$$

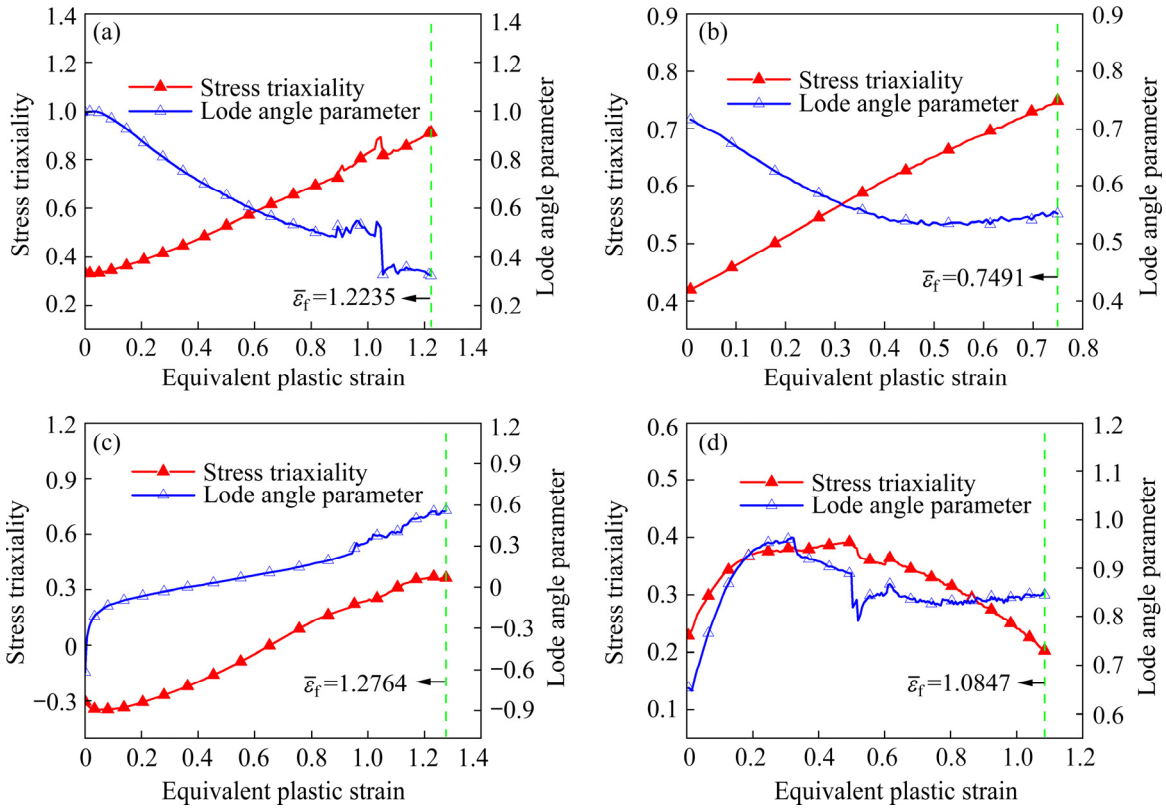

Fig. 4 Variation histories of stress triaxiality and Lode angle parameter at 0.03 s^{-1} and 453 K: (a) Flat smooth; (b) Arc notch; (c) Shear notch; (d) Tension−shear notch

$$\chi^2=\sum_{i=1}^{N}\frac{\left(\bar{\varepsilon}_{f,i}^{fit}-\bar{\varepsilon}_{f,i}^{exp}\right)^2}{\bar{\varepsilon}_{f,i}^{exp}} \tag{13}$$

$$\delta_r=\frac{1}{N}\sum_{i=1}^{N}\left|\frac{\bar{\varepsilon}_{f,i}^{fit}-\bar{\varepsilon}_{f,i}^{exp}}{\bar{\varepsilon}_{f,i}^{exp}}\right|\times 100\% \tag{14}$$

where δ_{mina} represents the minimum mean absolute error, χ^2 represents the Chi-square error, δ_r represents the mean relative error, $\bar{\varepsilon}_{f,i}^{fit}$ represents the fitting data, $\bar{\varepsilon}_{f,i}^{exp}$ represents the experimental data, and N represents the number of data.

Table 4 presents the mean relative errors for the different fracture models under different deformation conditions. As shown, the overall prediction accuracies of the modified McClintock and modified Cockcroft–Latham models were poor, with the calculated mean relative errors reaching 44.34% and 37.05%, respectively. The mean relative errors for the Bai–Wierzbicki and modified Wilkins models reached 14.27% and 9.94%, respectively. A comparative analysis indicated that the modified Wilkins model had the highest prediction accuracy.

4.2 Validation of fracture models

The modified Wilkins model was introduced into the finite element software ABAQUS/Explicit to predict the fracture behavior. Figure 5 presents a comparison between the finite element results and the experimental results at a strain rate of 0.03 s^{-1} and a temperature of 453 K. As shown, when the materials were damaged (the value of state variable SDV4 reached 1), the critical positions were all at the centers of the specimens, which is consistent with the experimental results. During the process from deformation to fracture, the coincidence degree of the simulated and experimental load–displacement curves for each specimen was high.

Table 5 presents a comparison of the load and displacement results at the time of fracture between the finite element simulation and the experiment. As shown, the mean relative error of the fracture displacement was 14.20%, and the mean relative error of the fracture load was 14.77%. Both mean relative errors were <15%. The modified Wilkins model can more accurately predict hot tensile deformation under different stress states.

Table 4 Mean relative errors for different fracture models

Strain rate/s^{-1}	Temperature/K	Mean relative error/%			
		Modified McClintock model	Modified Cockcroft–Latham model	Bai–Wierzbicki model	Modified Wilkins model
0.003	393	60.23	56.23	8.88	8.86
	423	75.74	71.98	20.84	11.85
	453	38.66	27.92	10.90	12.69
	483	34.19	26.76	29.32	17.05
0.01	393	38.87	33.12	6.08	2.87
	423	31.59	23.93	6.49	6.49
	453	43.70	34.03	18.82	8.69
	483	25.90	23.01	18.56	17.95
0.03	393	64.07	61.13	15.12	1.47
	423	37.16	28.93	6.77	2.75
	453	29.64	19.12	9.81	11.18
	483	30.61	15.20	10.36	10.96
0.1	393	52.29	48.55	27.49	10.17
	423	65.91	62.90	16.12	16.44
	453	53.14	44.38	12.84	9.68
	483	27.75	15.62	9.98	9.99

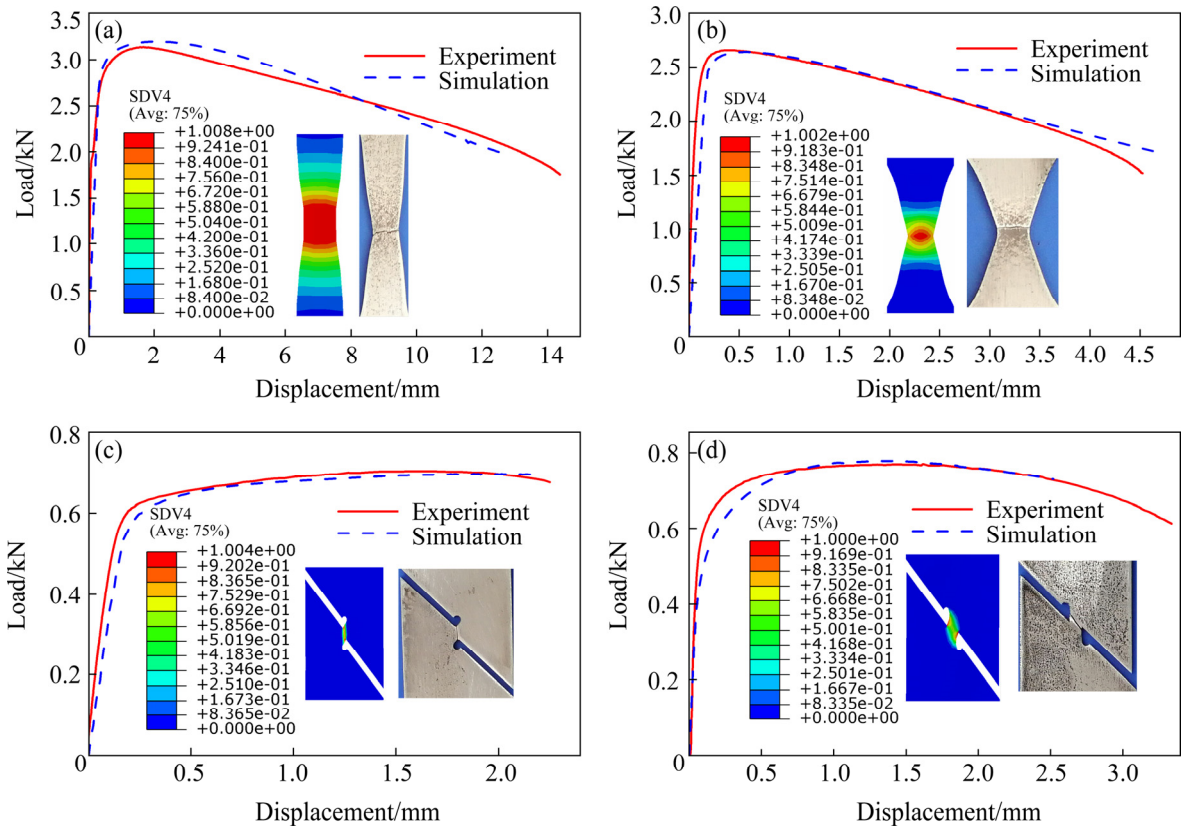

Fig. 5 Comparison of finite element simulation and experimental results at 0.03 s^{-1} and 453 K: (a) Flat smooth; (b) Arc notch; (c) Shear notch; (d) Tension−shear notch

Table 5 Accuracy comparison between simulation and experimental results

Specimen	Temperature/K	Fracture displacement			Fracture load		
		Experiment/mm	Simulation/mm	Error/%	Experiment/N	Simulation/N	Error/%
Flat smooth	393	8.4780	7.7573	8.50	3513.10	3761.35	7.07
	423	11.2136	12.2070	8.86	2674.10	2566.85	4.01
	453	14.3824	12.6565	12.00	1759.50	1979.12	12.48
	483	16.4579	13.9069	15.50	798.10	1332.98	67.02
Arc notch	393	2.4116	2.0499	15.00	3302.30	3394.52	2.79
	423	4.5570	4.7520	4.28	2169.40	2155.44	0.64
	453	4.5232	4.7025	3.96	1519.60	1703.09	12.07
	483	5.8076	5.7494	1.00	680.50	1064.52	56.43
Shear notch	393	0.9253	1.0360	11.97	954.30	966.84	1.31
	423	1.6153	1.9000	17.63	899.80	923.65	2.65
	453	2.2515	2.2065	2.00	676.30	696.99	3.06
	483	2.6132	1.8815	28.00	466.50	512.20	9.80
Tension−shear notch	393	1.9158	1.1676	39.05	1193.20	1218.94	2.16
	423	2.7360	2.4761	9.50	871.80	926.45	6.27
	453	3.3371	2.5195	24.50	612.70	730.35	19.20
	483	3.5795	2.6667	25.50	378.20	489.35	29.39

5 Hot drawing of cylindrical parts

5.1 Experiment and simulation

The geometric dimensions of the die used in the hot drawing experiment are shown in Fig. 6. The initial diameter of the sheet was 55 mm, and the lubricant was high temperature resistant nickel-based grease. The modified Wilkins model was introduced into ABAQUS/Explicit to simulate the hot drawing of cylindrical parts. The die size, sheet metal diameter, and boundary conditions were identical to those in the experiment. The sheet metal adopted was of an 8-node reduced integral solid element type.

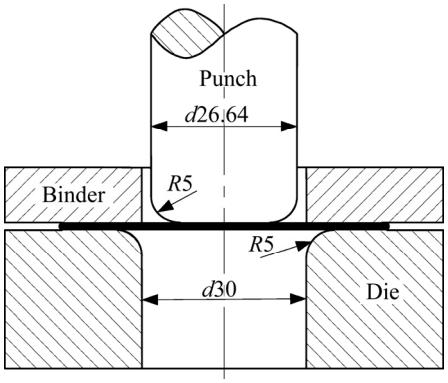

Fig. 6 Dimensions of hot drawing die (Unit: mm)

5.2 Hot drawing results

Hot drawing parts under different deformation conditions are presented in Fig. 7. As shown, the forming depth of the parts was shallow at the temperatures of 393 and 423 K. The rupture position of the parts was in the transition zone between the cylinder wall and the cylinder bottom, which was related to the plastic bending and the radial tensile stress state of the sheet in the fillet area of the punch. Additionally, this indicates that the plasticity of the magnesium alloys is poor at low temperatures. The forming depth increased with an increase in the temperature and a decrease in the speed. When the temperature reached 483 K, the parts were successfully pulled into the die, but there were bright scratch bands on the outer surface of the cylinder wall owing to the thickening of the flange and the change in the lubrication conditions.

The finite element simulation results under different deformation conditions are presented in Fig. 8. As shown, at 393 and 423 K, the fracture positions of the parts at the two speeds were identical to those in the experiment, and both were in the transition zone connecting the cylinder wall and the cylinder bottom, indicating that the fracture

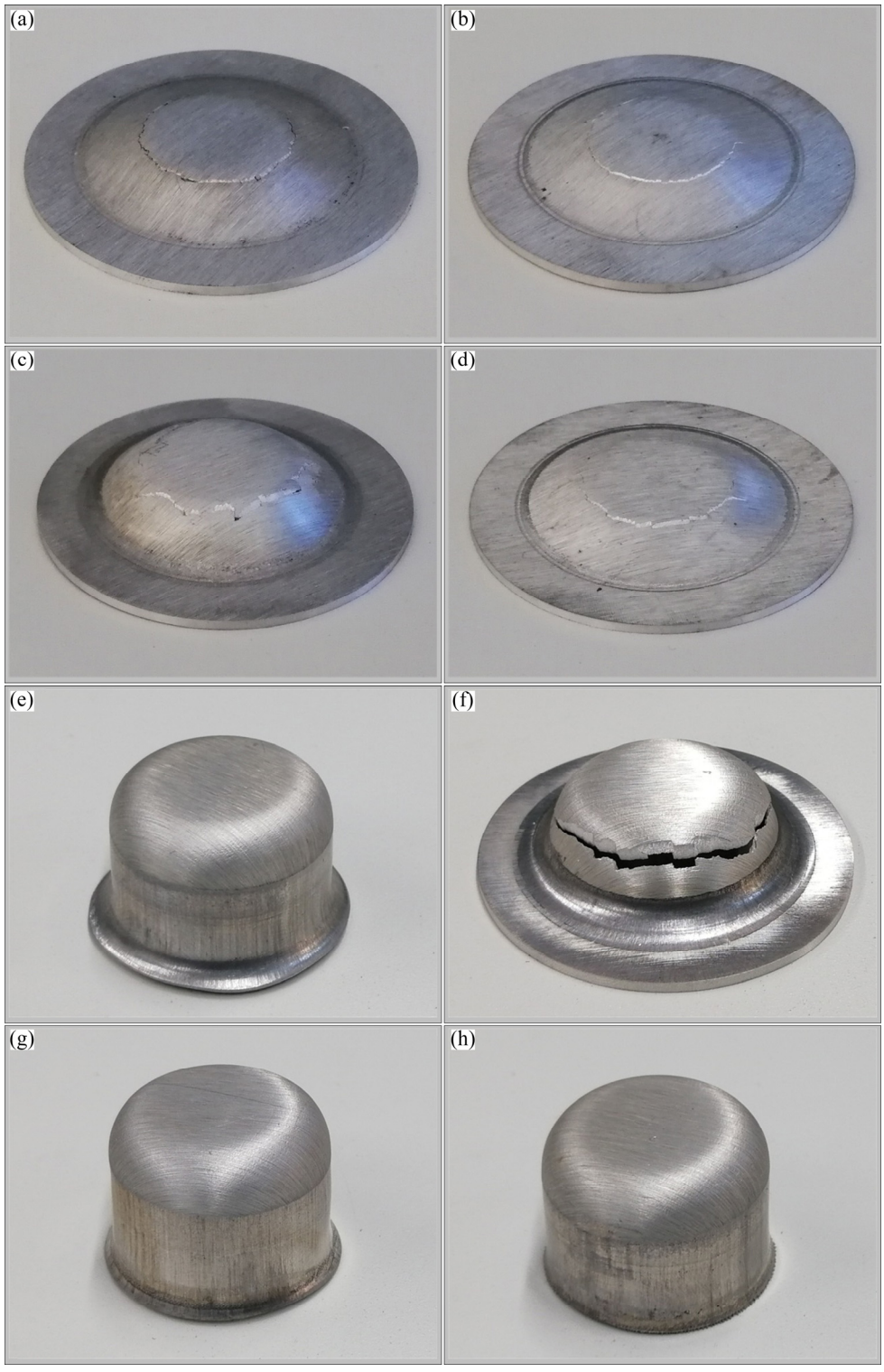

Fig. 7 Experimental parts for hot drawing under different deformation conditions: (a) 393 K, 1 mm/s; (b) 393 K, 3 mm/s; (c) 423 K, 1 mm/s; (d) 423 K, 3 mm/s; (e) 453 K, 1 mm/s; (f) 453 K, 3 mm/s; (g) 483 K, 1 mm/s; (h) 483 K, 3 mm/s

position predicted via the numerical simulation was accurate. As shown in Figs. 8(g, h), no fractures occurred in the parts, and the critical regions were consistent with those in the experiments.

Figure 9 presents a comparison of the forming depths between the finite element simulation and the experiment under different deformation conditions. As shown, the variation trends of the forming depth in the simulation and experiment were similar; the mean relative error was 13.88%.

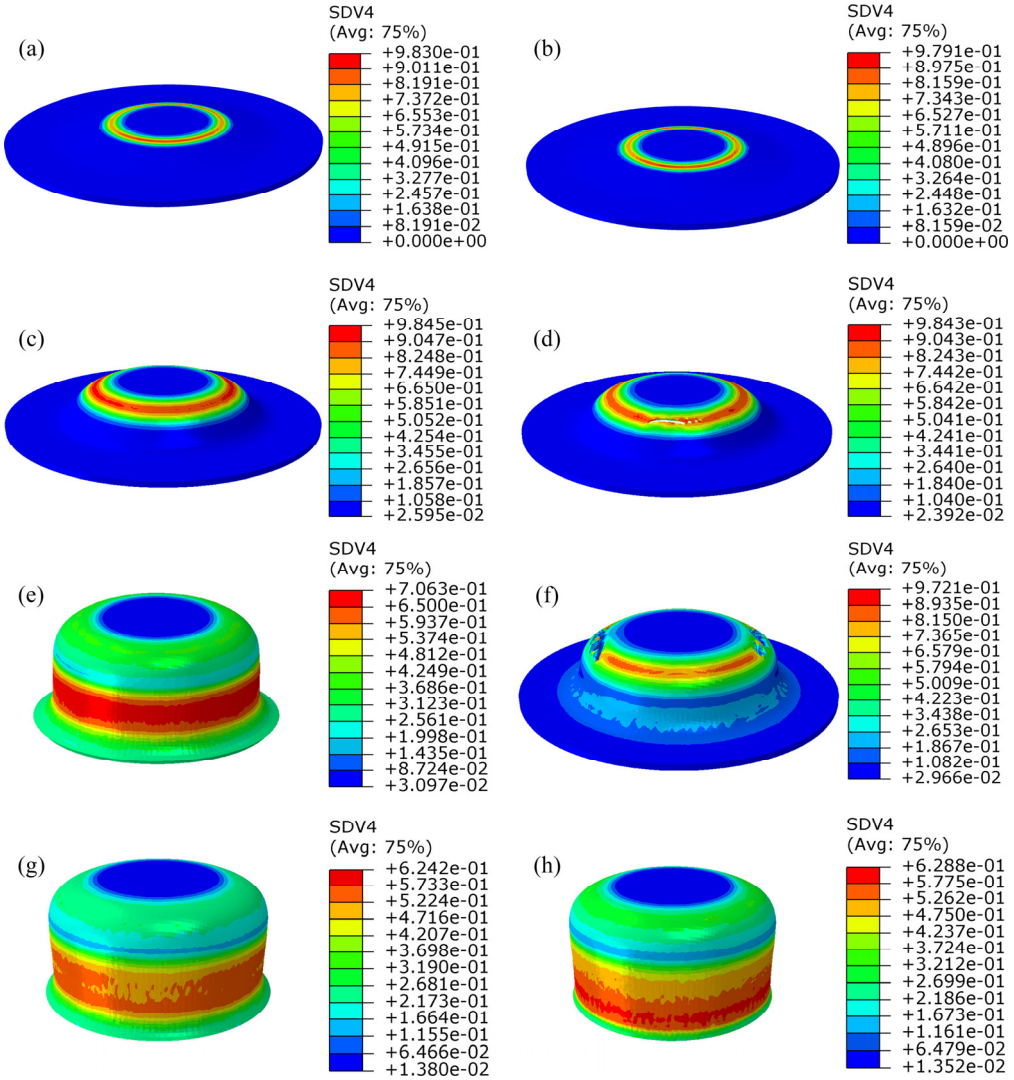

Fig. 8 Finite element simulation results for hot drawing under different deformation conditions: (a) 393 K, 1 mm/s; (b) 393 K, 3 mm/s; (c) 423 K, 1 mm/s; (d) 423 K, 3 mm/s; (e) 453 K, 1 mm/s; (f) 453 K, 3 mm/s; (g) 483 K, 1 mm/s; (h) 483 K, 3 mm/s

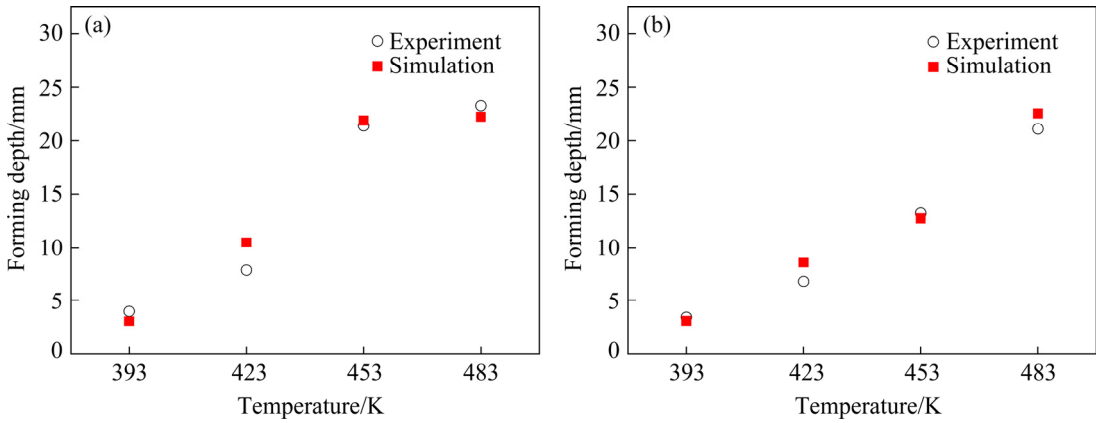

Fig. 9 Forming depth for hot drawing: (a) 1 mm/s; (b) 3 mm/s

At a low temperature of 393 K, the forming depths at the two speeds were <4 mm, indicating that the material was not sensitive to the speed at low temperatures. When the temperature reached 483 K, the forming effects at both speeds were better, and the effect of the temperature was dominant.

6 Conclusions

(1) According to the fracture data obtained under different deformation conditions, four fracture models were analyzed. It was determined that the fracture model with the highest prediction accuracy was the modified Wilkins model (mean relative error of 9.94%).

(2) The modified Wilkins model introduced into the finite element can effectively predict the hot tensile deformation under different stress states. The mean relative errors of the fracture displacement and fracture load were 14.20% and 14.77%, respectively.

(3) Based on the modified Wilkins model, the hot drawing of cylindrical parts was simulated by finite element method. A comparison with the experimental results indicated that the finite element method can accurately simulate the fracture process and predict the fracture location. The overall variation trends of the forming depth were similar between the simulation and the experiment, and the mean relative error was 13.88%.

Acknowledgments

The authors are grateful for the financial supports from the National Natural Science Foundation of China (No. 51705448), and the Natural Science Foundation of Hebei Province, China (No. E2021203163).

References

[1] WANG Bo-ning, WANG Feng, WANG Zhi, LIU Zheng, MAO Ping-li. Fabrication of fine-grained, high strength and toughness Mg alloy by extrusion-shearing process [J]. Transactions of Nonferrous Metals Society of China, 2021, 31(3): 666−678.

[2] BAHMANI A, ARTHANARI S, SHIN K S. Achieving a high corrosion resistant and high strength magnesium alloy using multi directional forging [J]. Journal of Alloys and Compounds, 2021, 856: 158077.

[3] LI Zhi-gang, YANG Hai-feng, LIU Jian-guang. Comparative study on yield behavior and non-associated yield criteria of AZ31B and ZK61M magnesium alloys [J]. Materials Science and Engineering A, 2019, 759: 329−345.

[4] MAGALHÃES D C C, KLIAUGA A M, SORDI V L. Flow behavior and fracture of Al−Mg−Si alloy at cryogenic temperatures [J]. Transactions of Nonferrous Metals Society of China, 2021, 31(3): 595−608.

[5] YANG Liu, DUAN Yong-chuan, GUAN Ying-ping, WANG Zhen-hua. Hot tensile deformation behavior and constitutive model of ZK61M high-strength magnesium alloy sheet [J]. Rare Metals, 2021, 40(5): 1182−1190.

[6] DONG Guo-jiang, CHEN Zhi-wei, YANG Zhuo-yun, FAN Bo-cheng. Comparative study on forming limit prediction of AA7075-T6 sheet with M−K model and Lou−Huh criterion [J]. Transactions of Nonferrous Metals Society of China, 2020, 30(6): 1463−1477.

[7] TANG Bing-tao, WU Fang-xing, WANG Qing-feng, LIU Ji-yuan, GUO Ning, GE Hai-long, WANG Qiao-ling, LIU Pei-xing. Damage prediction of hot stamped boron steel 22MnB5 with a microscopic motivated ductile fracture criterion: Experiment and simulation [J]. International Journal of Mechanical Sciences, 2019, 169: 105302.

[8] MORCHHALE A, BADRISH A, KOTKUNDE N, SINGH S K, KHANNA N, SAXENA A, NIKHARE C. Prediction of fracture limits of Ni−Cr based alloy under warm forming condition using ductile damage models and numerical method [J]. Transactions of Nonferrous Metals Society of China, 2021, 31(8): 2372−2387.

[9] HENSELER T, OSOVSKI S, ULLMANN M, KAWALLA R, PRAHL U. GTN model-based material parameters of AZ31 magnesium sheet at various temperatures by means of SEM in-situ testing [J]. Crystals, 2020, 10(10): 856.

[10] WANG Rui-ze, CHEN Zhang-hua, LI Yu-jie, DONG Chao-fang. Failure analysis of AZ31 magnesium alloy sheets based on the extended GTN damage model [J]. International Journal of Minerals Metallurgy and Materials, 2013, 20(12): 1198−1207.

[11] WEN Yue, CHEN Zhang-hua. Failure analysis of the tube hydroforming process based on anisotropic damage coupling model [J]. Journal of Mechanical Engineering, 2019, 55(18): 70–77.

[12] JIA Wei-tao, MA Li-feng, JIAO Ming-yang, LE Qi-chi, HAN Ting-zhuang, CHE Chao-jie. Fracture criterion for predicting edge-cracking in hot rolling of twin-roll casted AZ31 Mg alloy [J]. Journal of Materials Research and Technology, 2020, 9(3): 4773−4787.

[13] ARUN M S, CHAKKINGAL U. Workability limits of magnesium alloy AZ31B subjected to equal channel angular pressing [J]. Journal of Materials Engineering and Performance, 2018, 27(3): 1352−1360.

[14] SEOK Dong-yoon, KIM Daeyong, KIM Sang-woo, BAK Jeonghwan, LEE Young-seon, CHUNG Kwansoo. Fracture criterion for AZ31 Mg alloy sheet at elevated temperature [J]. Metals and Materials International, 2015, 21(1): 54−71.

[15] KIM Sang-woo, LEE Young-seon. Comparative study on failure prediction in warm forming processes of Mg alloy sheet by the FEM and ductile fracture criteria [J]. Metallurgical and Materials Transactions B, 2014, 45(2): 445−453.

[16] FAZILY P, YU Jeahyeong, LEE Chang-whan. Finite element analysis of blanking operation of magnesium alloy (AZ31) sheet using ductile fracture criteria and its experimental verification at various temperatures [J]. Journal of Physics: Conference Series, 2018, 1063: 012158.

[17] HUANG Xue-wei, GE Jian-zhou, ZHAO Jun, ZHAO Wei. A continuous damage model of Q690D steel considering the influence of Lode parameter and its application [J]. Construction and Building Materials, 2020, 262: 120067.

[18] WANG Xin-bao, DONG Xiang-huai. A void evolution model accounting for stress triaxiality, Lode parameter and effective strain for hot metal forming [J]. International Journal of Mechanical Sciences, 2020, 168: 105309.
[19] XIAO Yue, TANG Qi, HU Yu-mei, PENG Jian, LUO Wen-jun. Flow and fracture study for ZK60 alloy at dynamic strain rates and different loading states [J]. Materials Science and Engineering A, 2018, 724: 208−219.
[20] HABIB S A, LLOYD J T, MEREDITH C S, KHAN A S, SCHOENFELD S E. Fracture of an anisotropic rare-earth-containing magnesium alloy (ZEK100) at different stress states and strain rates: Experiments and modeling [J]. International Journal of Plasticity, 2019, 122: 285−318.
[21] KALE C, RAJAGOPALAN M, TURNAGE S, HORNBUCKLE B, DARLING K, MATHAUDHU S N, SOLANKI K N. On the roles of stress-triaxiality and strain-rate on the deformation behavior of AZ31 magnesium alloys [J]. Materials Research Letters, 2018, 6(2): 152−158.
[22] WANG Qiao-ling, BERTOLINI R, BRUSCHI S, GHIOTTI A. Anisotropic fracture behavior of AZ31 magnesium alloy sheets as a function of the stress state and temperature [J]. International Journal of Mechanical Sciences, 2019, 163: 105146.
[23] LEE Jeong-yeon, STEGLICH D, LEE Myoung-gyu. Fracture prediction based on a two-surface plasticity law for the anisotropic magnesium alloys AZ31 and ZE10 [J]. International Journal of Plasticity, 2018, 105: 1−23.
[24] ALI A N, HUANG Song-jeng. Ductile fracture behavior of ECAP deformed AZ61 magnesium alloy based on response surface methodology and finite element simulation [J]. Materials Science and Engineering A, 2019, 746: 197−210.
[25] XUE Zhen-yu, FALESKOG J, HUTCHINSON J W. Tension-torsion fracture experiments−Part II: Simulations with the extended Gurson model and a ductile fracture criterion based on plastic strain [J]. International Journal of Solids and Structures, 2013, 50(25/26): 4258−4269.
[26] ZHANG Qi, NIU Li-qun, LIANG Zheng-long, CAO Miao, ZHOU Tao. A porosity closure model considering stress triaxiality ratio and Lode stress parameter [J]. Journal of Materials Processing Technology, 2020, 286: 116824.
[27] BAI Y L, WIERZBICKI T. A comparative study of three groups of ductile fracture loci in the 3D space [J]. Engineering Fracture Mechanics, 2015, 135: 147−167.
[28] MCCLINTOCK F A. A criterion for ductile fracture by the growth of holes [J]. Journal of Applied Mechanics, 1968, 35(2): 363−371.
[29] OH S I, CHEN C C, KOBAYASHI S. Ductile fracture in axisymmetric extrusion and drawing−Part 2: Workability in extrusion and drawing [J]. Journal of Engineering for Industry, 1979, 101(1): 36−44.
[30] COCKCROFT M G, LATHAM D. Ductility and the workability of metals [J]. Journal Institute of Metals, 1968, 96(1): 33−39.
[31] BAI Y L,WIERZBICKI T. A new model of metal plasticity and fracture with pressure and Lode dependence [J]. International Journal of Plasticity, 2008, 24(6): 1071−1096.
[32] WILKINS M L. Mechanics of penetration and perforation [J]. International Journal of Engineering Science, 1978, 16(11): 793−807.
[33] SWIFT H W. Plastic instability under plane stress [J]. Journal of Mechanics Physics of Solids, 1952, 1(1): 1−18.
[34] ZHANG Ting-lian, YUAN Huang, YANG Shun. Fracture energy and tensile strength depending on stress triaxiality along a running crack front in three-dimensional cohesive modeling [J]. Engineering Fracture Mechanics, 2020, 227: 106919.
[35] JAIN N K, NANGIA U, JAIN J. A review of particle swarm optimization [J]. Journal of the Institution of Engineers, 2018, 99(4): 1−5.
[36] PARSOPOULOS K E, VRAHATIS M N. Recent approaches to global optimization problems through particle swarm optimization [J]. Natural Computing, 2002, 1(2/3): 235−306.

ZK61M 高强镁合金板热变形过程中的韧性断裂预测

杨 柳[1,2]，段永川[1,2]，官英平[1,2]

1. 燕山大学 先进锻压成形技术与科学教育部重点实验室，秦皇岛 066004；
2. 燕山大学 机械工程学院，秦皇岛 066004

摘 要：为了预测 ZK61M 高强镁合金板热变形过程的韧性断裂行为，在一定条件下进行实验和数值模拟。基于获得的各试件断口处的应力状态参数和断裂应变数据，采用粒子群优化算法求解 4 种断裂模型中的待定系数。依据误差评估结果，确定改进的 Wilkins 模型精度最高。将改进的 Wilkins 模型引入有限元中，并与实验进行对比。结果表明，预测的拉伸件断裂位移和断裂载荷的平均误差均小于 15%，预测的圆筒形件成形深度的平均误差为 13.88%，建立的有限元模型可以较为准确地模拟实验过程并预测断裂位置。

关键词：ZK61M 板；韧性断裂模型；参数优化；热变形；圆筒形件

(Edited by Bing YANG)